Time-Reversal SAR Imaging for Nondestructive Testing of Circular and Cylindrical Multi-Layered Dielectric Structures

Baolong Wu, Yuan Gao, Jaime Laviada, Mohammad Tayeb Ghasr, Senior member, *IEEE* and Reza Zoughi, Fellow, *IEEE*

Abstract—**In this paper, a synthetic aperture radar (SAR) approach, for imaging internal structures of generally lossy layered dielectric cylindrical objects, is presented. This method which properly accounts for different transmission and refraction path at each boundary between different layers, produces a properly focused image of embedded targets. This approach is also capable of addressing imaging needs for asymmetrical multi-layered cylindrical bodies. Consequently, this approach overcomes the limitation associated with the conventional methodology, in which free-space propagation is assumed. The calculation method of angular sampling criterion for circular and cylindrical SAR (i.e., circumferential and in height) are also presented. Electromagnetic simulations are performed on a three-layer cylindrical object, symmetrical and asymmetrical, with embedded targets to validate the approach. In addition, representative measurements are conducted at X-band (8.2-12.4 GHz) demonstrating the effectiveness of the approach for practical nondestructive evaluation applications.**

Index Terms—**Synthetic aperture radar (SAR), microwave imaging, circular SAR, cylindrical SAR, time reversal.**

I. INTRODUCTION

SYNTHETIC aperture radar (SAR) imaging techniques have been used for a number of applications including screening for concealed weapons, airport security, nondestructive inspection, and others [1]-[4]. Wideband SAR imaging techniques render high-resolution 3D and real-time images of objects and scenes, significantly contributing to their continued proliferation [5]-[6]. While for nondestructive testing (NDT) applications most of SAR imaging developments have involved planar structures, there is a great need to develop an imaging method that addresses inspection of cylindrical structures, such as pipes, holding tanks, etc.

For airborne SAR imaging systems circular scanning (i.e., circular synthetic aperture) enables viewing of an object or a scene from multiple views (angles), resulting in the approach known as circular SAR (C-SAR) [7]-[13]. For C-SAR which only scans an object circumferentially and does not scan along the height direction. Consequently, it is not able to provide better resolution along that direction. Many imaging approaches have been proposed based on Green's function, Fourier, back-projection and time reversal algorithms [7]-[8], [10]-[13]. Electromagnetic time reversal imaging algorithm has also been successfully used in a number of imaging applications, such as acousto-eletromagnetic wave interaction imaging, through wall imaging, to name a few [14]-[20].

When better resolution along the height direction is desired, then a cylindrical, rather than a circular scan one, must be performed [21]-[23]. This is commonly referred to as cylindrical SAR and is shown in Fig. 1a for a three-layer cylindrical composite structure. In this case, C-SAR simply refers to considering and analyzing a slice of the cylinder, as shown in Fig. 1b. Most C-SAR or cylindrical SAR applications consider free-space as the imaging domain. However, for many practical industrial applications, involving nondestructive testing of layered dielectric structures, such as pipes, made of plastics, fiberglass, high-density polyethylene (HDPE) and Polyvinyl chloride (PVC) that carry fluids and chemicals, this assumption no longer holds. If the free-space imaging background assumption is used for these cases, the resulting image will not be focused properly and the object of interest may not be identified all together. Commonly for these applications, the geometry of the layered cylinder (i.e., radii of layers, their dielectric properties, etc.) are known. Furthermore, for the materials mentioned above their dielectric properties fall in the category of low permittivity and low loss materials (for example see [24]-[25]). Consequently, for these specific applications the objective of inspection will be to localize an internal flaw or anomaly within the layered cylindrical structure. It must be noted that the method is applicable to any foreign

B. Wu is with the College of Computer Science and Electronic Engineering, Hunan University, China. (e-mail: wubaolongyou@163.com). J. Laviada is with the Department of Electrical Engineering, University of Oviedo, Gijón, 33203, Spain (e-mail: jlaviada@tsc.uniovi.es). Y. Gao, M.T. Ghasr and R. Zoughi are with the Applied Microwave Nondestructive Testing Laboratory (*amntl*), Missouri University of Science and Technology, Rolla, MO 65409 USA. (e-mail: [ygxgb][mtg7w6][Zoughi]@mst.edu).

object debris (FOD) that may find its way into such cylindrical bodies, as long as they have sufficient/measurable dielectric contrast with the host medium. However, to demonstrate the efficacy of the technique small cross-sectioned cylinders (in cross-section representing a point target) are used in this investigation.

A SAR approach based on modeling field propagation by Green's function for multi-layered planar media, implemented by efficient Wiener deconvolutions, has been demonstrated for nondestructive inspection and imaging purposes [4], [26], [27]. Green's function-based approach can also be used for multi-layered C-SAR and cylindrical SAR imaging. Although this is an efficient method, for a given layered structure its appropriate Green's function must first be derived, which often requires symmetric features in the structure (i.e. perfect cylinders). This approach has been successfully implemented for such cylindrical geometries [28]. After the Green's function has been computed, the computational cost of the approach (i.e., Wiener deconvolutions) is determined by $(PNM \log(NM))$, where N and M are the total number of points along the height and azimuth directions, respectively, and P is the total number of concentric rings (i.e., radial) considered to build the image. However, using time reversal imaging approach does not have this geometrical constraint (i.e., symmetry requirement) and is more general, and can be readily extended to arbitrary measurement and object shape domains, even though it may not be as computationally as efficient. This important feature will be illustrated in Section III. A time reversal C-SAR imaging approach based on Fermat's principle has been proposed for human head and body imaging, which is considered as a two-layer lossless structure [29]-[30]. However, to the best of authors' knowledge, C-SAR and cylindrical SAR imaging for a generally lossy and multi-layered structure use of this method have not been reported.

In this paper the method for calculating the forward transmission and refraction paths of electromagnetic waves in a generally lossy cylindrically multi-layer structure is proposed. Then, time reversal imaging algorithm is used to obtain SAR image of the multi-layer circular and cylindrical structure. Multiple reflections have not been included in the analysis. If the layer to-be-imaged is made of a lossy material, or if the permittivity contrast between layers is not large then the multiple reflections will be negligible and are not considered in this paper. In addition, if there are many high lossy layers, the absorption of each layer would be strong enough such that it would limit the penetration depth and image deeper layer. However, the method proposed in this paper could be used to general cases without the extreme cases discussed above. Moreover, in contrast to other approaches such as the Green's function scheme, it provides for analyzing nonconcentric (i.e., asymmetrical) cylinders. Since the transmission/refraction/reflection model used in this paper is based on Snell's law, which is formulated for the interface of homogenous media, the presented approach is only valid for layers made of homogenous material. However, it is important to note that this homogeneous layered model encompasses most of the standard nondestructive evaluation applications. A discussion of the sampling criterion is also provided.

II. THEORETICAL FOUNDATION

This section which comprises of three parts outlines the derivations of proposed method is parts A and B. The former elaborates the details of the transmission and refraction models for multi-layer circular and cylindrical structures. The latter, shows how time reversal algorithm given in part B is incorporated into the model in part A for obtaining the final image. Part C outlines the sampling criteria of the proposed method.

A. Transmission and Refraction Models for Multi-Layer Circular and Cylindrical Structures

Fig. 1a shows a cylindrical structure made of three generally lossy dielectric layers. As shown, an antenna/probe is used to measure the reflection coefficient along the height and around the cylinder (as also done in the experiment described later). The corresponding circular version of this structure (i.e., a slice through the cylinder) is shown in Fig. 1b. The three-layer structure, as shown in Fig.1b, will be analyzed first. Then, the formulation is expanded to the cylindrical case (i.e., Fig. 1a). In Fig. 1b, S_1 represents one of the measurement points, P represents a point target located in the third layer and O is the center position of the circular structure. Each layer represents a generally lossy dielectric
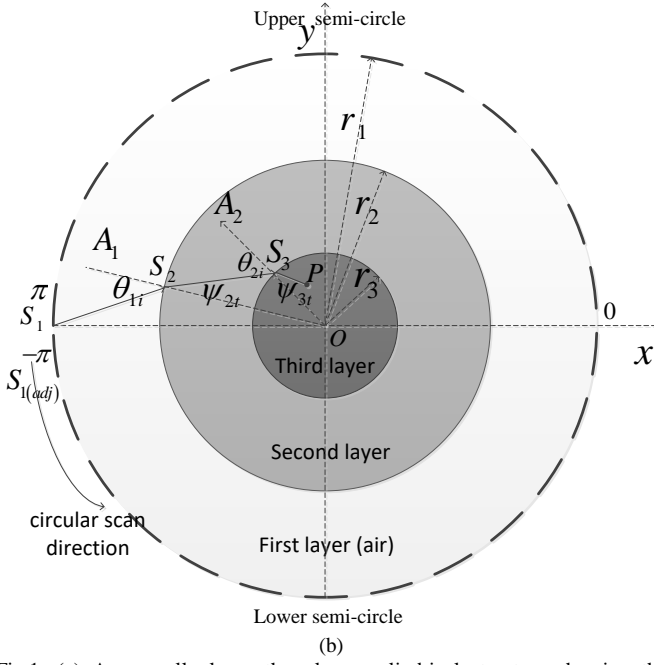

(a)
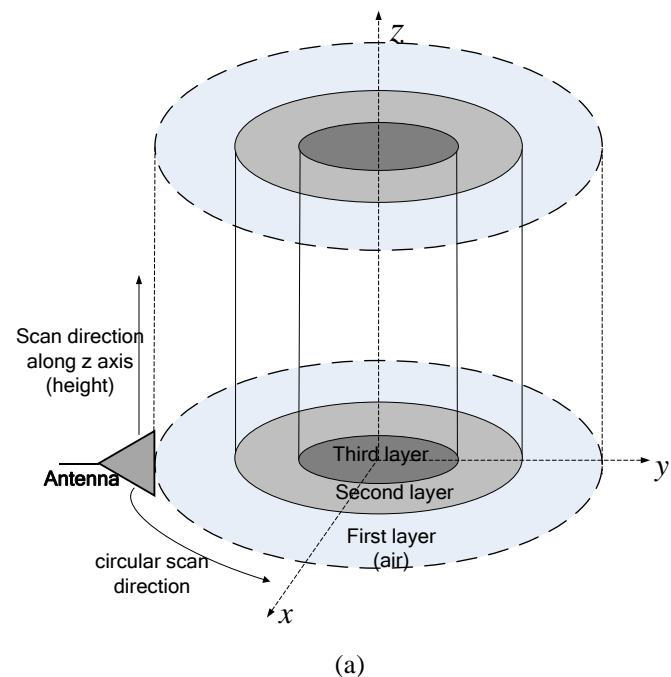
Fig.1: (a) A generally lossy three-layer cylindrical structure showing the schematic for two scan directions (cylindrical SAR), and (b) scan schematic of a circular slice of the cylindrical structure (C-SAR).

(non-magnetic) material with a relative (to free-space) complex dielectric constant of ε_1, ε_2, ε_3, and a radius of r_1, r_2 and r_3, respectively. Almost always in practical applications the first layer is air (free-space) in which a measurement probe scans the structure (i.e., the measurement domain).

Since the dielectric constant of each layer is different, an incident signal undergoes refraction and reflection at each boundary. As mentioned above, (multiple) reflections are not considered in this work. Let us denote the incidence angle and the true refraction angle (as defined in [31]) at the boundary between the first and the second layer as θ_{1i} and ψ_{2t}, respectively. In a similar fashion, the incidence angle and true refraction angle at the boundary between the second and the third layers are denoted as θ_{2i} and ψ_{3t}, respectively. The complex propagation constant in each layer is given by:

$$\gamma_m = j\omega\sqrt{\mu_m \varepsilon_m} = \alpha_m + j\beta_m \tag{1}$$

where ω is the angular frequency, α and β are the phase and attenuation constants in each layer, m represents the m th layer. According to Snell's law of refraction, we also have [31]:

$$\gamma_1 \sin\theta_{1i} = \gamma_2 \sin\theta_{2t} \tag{2}$$

$$\gamma_2 \sin\theta_{2i} = \gamma_3 \sin\theta_{3t} \tag{3}$$

and

$$\cos\theta_{2t} = \sqrt{1-\sin^2\theta_{2t}} = s_1\left(\cos\xi_1 + j\sin\xi_1\right) \tag{4}$$

$$\cos\theta_{3t} = \sqrt{1-\sin^2\theta_{3t}} = s_2\left(\cos\xi_2 + j\sin\xi_2\right) \tag{5}$$

where θ_{2t} is the complex refraction angle between the first and second layer, θ_{3t} is the complex refraction angle between the second and third layer. s_1 and s_2 represent the amplitude of

$\cos\theta_{2t}$ and $\cos\theta_{3t}$ respectively. ξ_1 and ξ_2 represent the phase of $\cos\theta_{2t}$ and $\cos\theta_{3t}$ respectively. If two neighborhood layers both are lossless materials, the corresponding complex refraction angle between them will be equal to true refraction angle, otherwise it is not. Let

$$q_1 = s_1\left(\alpha_1\cos\xi_1 + \beta_1\sin\xi_1\right) \tag{6}$$

$$q_2 = s_2\left(\alpha_2\cos\xi_2 + \beta_2\sin\xi_2\right) \tag{7}$$

$$u_1 = \beta_1\sin\theta_{1i} \tag{8}$$

$$u_2 = \beta_2\sin\theta_{2i}. \tag{9}$$

The true refraction angle between each two layers is given by [31]:

$$\psi_{2t} = \tan^{-1}\left(u_1 / q_1\right) \tag{10}$$

$$\psi_{3t} = \tan^{-1}\left(u_2 / q_2\right). \tag{11}$$

In practice, the transmission path from S_1 to P is unknown and needs to be calculated so that the total phase shift can be estimated at each frequency in order to apply the time-reversal imaging method, which will be described in the next section. Thus, the problem of finding the corresponding intersection points S_2 and S_3 must be firstly solved. Let:

$$\hat{S}_2 = \left(r_2\cos\hat{\varphi}_2, r_2\sin\hat{\varphi}_2\right), \hat{\varphi}_2 \in [-\pi, \pi) \tag{12}$$

$$\hat{S}_3 = \left(r_3\cos\hat{\varphi}_3, r_3\sin\hat{\varphi}_3\right), \hat{\varphi}_3 \in [-\pi, \pi) \tag{13}$$

where $\hat{s}_2$ and $\hat{s}_3$ are the position functions with respect to the variables $\hat{\varphi}_2$, $\hat{\varphi}_3$. Let us denote the angle between the vector line $\overrightarrow{\hat{S}_2\hat{S}_3}$ and $\overrightarrow{\hat{S}_2 O}$ by $\hat{\psi}_{2t}$, the angle between the vector line $\overrightarrow{\hat{S}_3 P}$ and $\overrightarrow{\hat{S}_3 O}$ by $\hat{\psi}_{3t}$, the angle between the vector line $\overrightarrow{\hat{S}_2 S_1}$ and $\overrightarrow{\hat{S}_2 A_1}$ by $\hat{\theta}_{1i}$, the angle between the vector line $\overrightarrow{\hat{S}_3\hat{S}_2}$ and $\overrightarrow{\hat{S}_3 A_2}$ by $\hat{\theta}_{2i}$. Next, replacing θ_{1i} and θ_{2i} with $\hat{\theta}_{1i}$ and $\hat{\theta}_{2i}$ respectively in (2) and (3), then using (2)-(11), finally we can obtain $\psi_{2t}\left(\hat{\theta}_{1i}\right)$ and $\psi_{3t}\left(\hat{\theta}_{2i}\right)$, which corresponds to $\hat{\theta}_{1i}$ and $\hat{\theta}_{2i}$. Define the following cost function F,

$$F = \left(\psi_{2t}\left(\hat{\theta}_{1i}\right) - \hat{\psi}_{2t}\right)^2 + \left(\psi_{3t}\left(\hat{\theta}_{2i}\right) - \hat{\psi}_{3t}\right)^2. \tag{14}$$

$\psi_{2t}\left(\hat{\theta}_{1i}\right)$, $\psi_{3t}\left(\hat{\theta}_{2i}\right)$, $\hat{\psi}_{2t}$ and $\hat{\psi}_{3t}$ all are functions of the two variables $\hat{\varphi}_2$ and $\hat{\varphi}_3$. So F is also the function with the two variables $\hat{\varphi}_2$ and $\hat{\varphi}_3$. Once (14) is minimized, it results in the best estimated real transmission positions at the boundaries between different layers, such that:

$$\left(S_{2(est)}, S_{3(est)} \right) = find \left(\min_{\hat{S_2}\left(\hat{\varphi_2}\right),\hat{S_3}\left(\hat{\varphi_3}\right)} F \right) \qquad (15)$$

where $S_{2(est)}$ is the estimated transmission position at the boundary between the first layer and second layer, $S_{3(est)}$ is the estimated transmission position at the boundary between the second layer and third layer. Solving (15) means that we should find the estimated real transmission positions at the boundaries between different layers, i.e. $S_{2(est)}$ and $S_{3(est)}$ which are related to the two-variable $\hat{\varphi_2}$, $\hat{\varphi_3}$ which results in minimizing F (for example, using Levenberg-Marquardt algorithm). Subsequently, solving (15) becomes a two-variable optimization problem. For the half-circle sub-aperture (π rad) nearer to the pixel to-be-imaged, (15) must at most result in one solution. For the remaining half-circle sub-aperture (π rad) farther from the pixel to-be-imaged, there may exist a few cases with multiple solutions or transmission paths (i.e., up to three) for a given set of radii, dielectric constants of each layer and positions to-be-imaged. In some cases, no solution may exist for both half-circles. The number of solutions depends on the dielectric constant and radius of each layer and the specific position to be imaged. Therefore, practically we may need to consider all possible solutions. In order to remedy this issue, we can set several different initial possible transmission paths from which to begin the search. After calculating the transmission positions through different layers, the transmission paths from S_1 to P are directly obtained.

The transmission coefficients at the boundaries between different layers, which are also required by the time-reversal algorithm detailed in the next section, are calculated as follows [31].

$$\tau_{mn\perp} = \left(2\eta_n \cos\theta_{mi}\right)/\left(\eta_n \cos\theta_{mi} + \eta_m \cos\theta_{nt}\right) \qquad (16)$$

$$\tau_{mn\parallel} = \left(2\eta_n \cos\theta_{mi}\right)/\left(\eta_n \cos\theta_{nt} + \eta_m \cos\theta_{mi}\right) \qquad (17)$$

where $\eta_m = \sqrt{\mu_m / \varepsilon_m}$ is the intrinsic impedance of a given layer (m th layer), and τ_{mn} is the transmission coefficient at the boundary of the m th and n th layers, while "$\perp$" and "$\parallel$" represent perpendicular and parallel polarizations, respectively. Considering the two-way travel associated with the incident signal, we have:

$$\tau_{mn\perp(round-trip)} = \left(2\eta_n \cos\theta_{mi} 2\eta_m \cos\theta_{nt}\right)/\left(\eta_n \cos\theta_{mi} + \eta_m \cos\theta_{nt}\right)^2 \qquad (18)$$

$$\tau_{mn\parallel(round-trip)} = \left(2\eta_n \cos\theta_{mi} 2\eta_m \cos\theta_{nt}\right)/\left(\eta_n \cos\theta_{nt} + \eta_m \cos\theta_{mi}\right)^2 \qquad (19)$$

Assuming the transmitted signal at the measurement point S_1 is E and the reflection from the point target P is denoted as P_r, the received signal from the point target P received at S_1 is then:

$$S_{1P(rec)\perp} = E_\perp P_{\perp r} \tau_{12\perp(round-trip)} \tau_{23\perp(round-trip)} \exp\left(-j2\left(k_1 \left|\overrightarrow{S_1 S_2}\right|\right.\right.$$
$$\left.\left. +k_2 \left|\overrightarrow{S_2 S_3}\right| + k_3 \left|\overrightarrow{S_3 P}\right|\right)\right) \qquad (20)$$

$$S_{1P(rec)\parallel} = E_\parallel P_{\parallel r} \tau_{12\parallel(round-trip)} \tau_{23\parallel(round-trip)} \exp\left(-j2\left(k_1 \left|\overrightarrow{S_1 S_2}\right|\right.\right.$$
$$\left.\left. +k_2 \left|\overrightarrow{S_2 S_3}\right| + k_3 \left|\overrightarrow{S_3 P}\right|\right)\right) \qquad (21)$$

where "$\left|\overrightarrow{}\right|$" represents the norm of the corresponding vector, $k_m = \omega\sqrt{\mu_m \varepsilon_m}$ is the wavenumber of a given layer (m th layer). So when the measurement and point target positions are fixed, the corresponding received signal can be calculated using (20) and (21). For the case of multiple transmission paths, we need to coherently add them after calculating each transmission path using (20) and (21).

For the cylindrical structure shown in Fig.1a, we must also search for the transmission positions along the z direction and at the boundaries through different layers. Thus, (12) and (13) are extended to include z, as follows:

$$\hat{S_2} = \left(r_2 \cos\hat{\varphi_2}, r_2 \sin\hat{\varphi_2}, \hat{z_2} \right), \hat{\varphi_2} \in [-\pi, \pi) \qquad (22)$$

$$\hat{S_3} = \left(r_3 \cos\hat{\varphi_3}, r_3 \sin\hat{\varphi_3}, \hat{z_3} \right), \hat{\varphi_3} \in [-\pi, \pi) \qquad (23)$$

Now, (14) becomes a function with respect to four variables $\hat{\varphi_2}$, $\hat{\varphi_3}$, $\hat{z_2}$ and $\hat{z_3}$. By minimizing this function, as shown in (24), we can find the transmission positions at the boundaries through different layers for this cylindrical case.

$$\left(S_{2(est)}, S_{3(est)} \right) = \min_{\hat{\varphi_2},\hat{\varphi_3},\hat{z_2},\hat{z_3}} F \qquad (24)$$

For a general N-layer asymmetric circular structure, we can use the same principle to obtain the transmission and refraction expressions. Assuming the object of interest to-be-imaged is located in the N-th layer (the innermost layer), (14) becomes a function with N-1 variables, and solving (15) will become an optimization problem with N-1 variables. For one transmission path from the measurement point S_1 to the point target P in a general N-layer cylindrical structure, let

$$l_{1(rec)\perp} = P_{\perp r} \tau_{12\perp(round-trip)} \tau_{23\perp(round-trip)} \cdots \tau_{N-1N\perp(round-trip)}$$
$$\exp\left(-j2\left(k_1 \left|\overrightarrow{S_1 S_2}\right| + k_2 \left|\overrightarrow{S_2 S_3}\right| + k_3 \left|\overrightarrow{S_3 S_4}\right| + ... + k_N \left|\overrightarrow{S_N P}\right|\right)\right) \qquad (25)$$

$$l_{1(rec)\parallel} = P_{\parallel r} \tau_{2\parallel(round-trip)} \tau_{3\parallel(round-trip)} \cdots \tau_{N\parallel(round-trip)} \exp$$
$$\left(-j2\left(k_1 \left|\overrightarrow{S_1 S_2}\right| + k_2 \left|\overrightarrow{S_2 S_3}\right| + k_3 \left|\overrightarrow{S_3 S_4}\right| + ... + k_N \left|\overrightarrow{S_N P}\right|\right)\right) \qquad (26)$$

For a 3D cylindrical structure, the polarization vector must be resolved into in-plane and normal components, each depending on the local relative geometry and the incident wave number. For such a case, refraction is then represented by a tensor that is applied to the incident polarization vector, to calculate the transmitted polarization vector. Finally, the received signal from point target P at the measurement point S_1 for a general N-layer cylindrical structure becomes:

This article has been accepted for publication in a future issue of this journal, but has not been fully edited. Content may change prior to final publication. Citation information: DOI 10.1109/TIM.2019.2918371, IEEE Transactions on Instrumentation and Measurement

> REPLACE THIS LINE WITH YOUR PAPER IDENTIFICATION NUMBER (DOUBLE-CLICK HERE TO EDIT) <　　5

$$\left[S_{1P(rec)\perp}, S_{1P(rec)\|}\right] = \begin{bmatrix} a_{\perp\perp}E_{\perp}, a_{\perp\|}E_{\perp} \\ a_{\|\perp}E_{\|}, a_{\|\|}E_{\|} \end{bmatrix} \begin{bmatrix} l_{1(rec)\perp} \\ l_{1(rec)\|} \end{bmatrix} \quad (27)$$

where a (a real number) represents the decomposed coefficient along the parallel and perpendicular direction.

For any other measurement points and positions to-be-imaged, the transmission path can be calculated using the same method. Therefore, for a given frequency, once the number of layers of the cylindrical structure, the complex dielectric constant, radius and axis offset of each layer are known, the transmission path and the received signal model for each measurement point and position to-be-imaged can be calculated.

B.　Time Reversal Imaging Method

After formulating the transmission path and received signal model for each measurement point and positions to-be-imaged, we can use time reversal imaging method to obtain SAR images of circular and cylindrical structures. For 2-D C-SAR imaging, let:

$$S_{1ref}\left(x_i, y_j, \varphi_1\right) = \Big[\tau_{2(round-trip)}\tau_{3(round-trip)}\cdots\tau_{N(round-trip)}$$
$$\exp\left(-j2\left(k_1\left|\overrightarrow{S_1S_2}\right| + k_2\left|\overrightarrow{S_2S_3}\right| + k_3\left|\overrightarrow{S_3S_4}\right| + \ldots + k_N\left|\overrightarrow{S_NP}\right|\right)\right)\Big]_{(x_i, y_j, \varphi_1)}$$
$$(28)$$

where $S_{1ref}\left(x_i, y_j, \varphi_1\right)$ is the reference signal with respect to the variables x_i, y_j and φ_1. $\left(x_i, y_j\right)$ represents the position to-be-imaged (i.e. P), where the aspect angle of the measurement points, φ_1, is measured from the x-axis to the measurement point, (S_1) in Fig. 1b. So, φ_1, is between (0, π) and (0, $-\pi$) for the upper and lower semi-circles in Fig. 1b, respectively. Considering polarization, we need to use $\tau_{n\perp(round-trip)}$ or $\tau_{n\|(round-trip)}$ to replace $\tau_{n(round-trip)}$ in (28). The final image of the innermost layer will then be given by:

$$f\left(x_i, y_j\right) = \sum_{\varphi_1} S_{1(rec)}\left(\varphi_1\right) S_{1ref}^*\left(x_i, y_j, \varphi_1\right) \quad (29)$$

where $f\left(x_i, y_j\right)$ is the value at position $\left(x_i, y_j\right)$, $S_{1(rec)}\left(\varphi_1\right)$ is the received signal measured at the angle φ_1 and the superscript "*" denotes conjugate.

Therefore, for a generally lossy and multi-layered 2D circular structure, we can use (28) and (29) to accurately reconstruct the SAR image. For 3D multi-layered cylindrical structure, due to the complicated tensor representation of polarization vectors, we can use the following method to simplify the model and to obtain a closely representative image of the structure. In general, for a multi-layered low-loss structure, the imaginary part of the material permittivity is much smaller than the real part. Therefore, τ in (18) and (19) becomes nearly a real number and the phase part of τ is approximately equal to 0. Since SAR imaging relies on the constructive coherent addition to form an image, only on the phase change due to travel time, not the amplitude of the signal, becomes critical and as such τ and a in (27) need not be considered. Thus for 3D cylindrical SAR

imaging, the reference signal could be built as follow:

$$S_{1ref}\left(x_i, y_j, z_k, Z_{mea}, \varphi_1\right) = \Big[\exp\left(-j2\left(k_1\left|\overrightarrow{S_1S_2}\right|\right.\right.$$
$$\left.\left.+ k_2\left|\overrightarrow{S_2S_3}\right| + k_3\left|\overrightarrow{S_3S_4}\right| + \ldots + k_N\left|\overrightarrow{S_NP}\right|\right)\right)\Big]_{(x_i, y_j, z_k, Z_{mea}, \varphi_1)} \quad (30)$$

where $S_{1ref}\left(x_i, y_j, z_k, Z_{mea}, \varphi_1\right)$ is the reference signal with respect to the variables x_i, y_j, z_k, Z_{mea}, and φ_1. $\left(x_i, y_j, z_k\right)$ represents the position to-be-imaged, and the aspect angle of the measurement points. Z_{mea} represents the position of the measurement points along height the z-direction. The final image of the innermost layer will then be given by:

$$f\left(x_i, y_j, z_k\right) = \sum_{Z_{mea}}\sum_{\varphi_1} S_{1(rec)}\left(Z_{mea}, \varphi_1\right)\bullet S_{1ref}^*\left(x_i, y_j, z_k, Z_{mea}, \varphi_1\right)$$
$$(31)$$

where $f\left(x_i, y_j, z_k\right)$ is the value at position $\left(x_i, y_j, z_k\right)$, $S_{1(rec)}\left(Z_{mea}, \varphi_1\right)$ is the received signal measured at the angle φ_1 and the position Z_{mea} along the z-direction.

C.　Sampling Criterion for Multi-Layer Circular and Cylinder SAR

For multi-layer C-SAR, assuming $S_{1(adj)}$ is the adjacent measurement point to its previous measurement point S_1, let:

$$S_{1(adj)(rec)} = \vec{E}\tau_{2(adj)(round-trip)}\tau_{3(adj)(round-trip)}\cdots\tau_{N(adj)(round-trip)}$$
$$\exp\left(-j2\left(k_1\left|\overrightarrow{S_{1(adj)}S_{2(adj)}}\right| + k_2\left|\overrightarrow{S_{2(adj)}S_{3(adj)}}\right|\right.\right.$$
$$\left.\left.+ k_3\left|\overrightarrow{S_{3(adj)}S_{4(adj)}}\right| + \ldots + k_N\left|\overrightarrow{S_{N(adj)}P}\right|\right)\right) \quad (32)$$

where $S_{1(adj)(rec)}$ is the received signal from the target position P (located in the innermost layer) measured at the position of $S_{1(adj)}$. Defining the following function which represents the phase difference between two consecutive sampling points with respect to the variables x_i, y_j, φ_1 and φ_{1sp}, we get:

$$G\left(x_i, y_j, \varphi_1, \varphi_{1sp}\right) = \left|\angle\left(\exp\left(j\angle\left(S_{1(rec)}\right)\right)\exp\left(-j\right.\right.\right.$$
$$\left.\left.\left.\angle\left(S_{1(adj)(rec)}\right)\right)\right)\right|_{(x_i, y_j, \varphi_1, \varphi_{1sp})} = \left|\angle\left(\exp\left(j\angle\left(S_{1(ref)}\right)\right)\right.\right. \quad (33)$$
$$\left.\left.\exp\left(-j\angle\left(S_{1(adj)(ref)}\right)\right)\right)\right|_{(x_i, y_j, \varphi_1, \varphi_{1sp})}$$

where "$\angle$" represents angle calculation operation of the corresponding complex number, and $\left(x_i, y_j\right)$ is the object target position to-be-imaged. $\varphi_1 \in \left[-\pi, \pi\right)$ represents the aspect angle of the measurement point S_1, $S_{1(adj)(ref)}$ is the reference signal associated with $S_{1(adj)(rec)}$, and φ_{1sp} is the angular sampling step between two adjacent measurement

points. Defining the following function with respect to the variable φ_{1sp}, we get:

$$H\left(\varphi_{1sp}\right) = \max_{x_i, y_j, \varphi_1} G\left(x_i, y_j, \varphi_1, \varphi_{1sp}\right) \tag{34}$$

where $H\left(\varphi_{1sp}\right)$ represents the maximum value of $G\left(x_i, y_j, \varphi_1, \varphi_{1sp}\right)$ for all of x_i, y_j and φ_1 when the angular sampling step space is fixed at φ_{1sp}. In order to reconstruct the image of innermost layer without spatial frequency aliasing, according to the Nyquist sampling criterion, the angular sampling step space of measurement points must meet the following condition:

$$H\left(\varphi_{1sp}\right) \le \pi . \tag{35}$$

Equation (34) is a monotonically decreasing function with respect to the variable φ_{1sp}, so the largest angle sampling step space of measurement points for reconstructing the image of innermost layer without loss is the solution of the following:

$$H\left(\varphi_{1sp}\right) = \pi . \tag{36}$$

Let $\varphi_{1sp(critical)}$ be the solution to (36). Then, if $\varphi_{1sp} < \varphi_{1sp(critical)}$, we have an "over-sampled" case. Otherwise, if $\varphi_{1sp} > \varphi_{1sp(critical)}$, we have an "under-sampled" case. In practical applications, we need to use the over-sampling number of the measurement points for imaging if we want to prevent spatial frequency aliasing. Similarly, for a multi-layer cylindrical SAR case, (34) will be extended, as follows:

$$H\left(\varphi_{1sp}, Z_{sp}\right) = \max_{x_i, y_j, z_k, Z_{mea}, \varphi_1} G\left(x_i, y_j, z_k, Z_{mea}, \varphi_1, \varphi_{1sp}, Z_{sp}\right) \tag{37}$$

where $H\left(\varphi_{1sp}, Z_{sp}\right)$ represents the maximum value of $G\left(x_i, y_j, z_k, Z_{mea}, \varphi_1, \varphi_{1sp}, Z_{sp}\right)$ when the angular sampling step space and sampling step space along z-direction are fixed at φ_{1sp}, Z_{sp}, respectively. The largest angular sampling step space and sampling step space along z-direction of the measurement points for properly reconstructing the image of the innermost layer without aliasing is the solution of the following:

$$H\left(\varphi_{1sp}, Z_{sp}\right) = \pi . \tag{38}$$

Let, $\left(\varphi_{1sp(critical)}, Z_{sp(critical)}\right)$ is the solution of (38). If $\varphi_{1sp} < \varphi_{1sp(critical)}$, $Z_{sp} < Z_{sp(critical)}$, we have an over-sampled case. Otherwise, if $\varphi_{1sp} > \varphi_{1sp(critical)}$, $Z_{sp} > Z_{sp(critical)}$, we have an under-sampled situation.

If the object to-be imaged is in free-space (i.e., no layered structure case), we can obtain the analytical solutions for (36) and (38), as in [32]. In this case, using these analytical expressions, the critical sampling space can be calculated directly once the radii of scanning aperture and imaging domain are known. For the general case of a multi-layer medium, no analytical expression for (36) and (38) can be obtained, in which case (36) and (38) must be evaluated numerically. In practical applications, due to the large computational cost for

solving (36) and especially (38), we can start with an initial guess for the sampling steps, as long as it meets the sampling criterion in (35).

In addition, for the half-circle sub-aperture farther from the location to-be-imaged, it is not easy to define and evaluate the sampling criterion since multiple (i.e., two or three) solutions may exist, as discussed in Section II-A. So we just apply this sampling criterion into the half-circle sub-aperture nearer to the location to-be-imaged and ensure this half-circle sub-aperture is over-sampled.

The above analysis is for the target to-be-imaged which is located in the innermost layer. For a target in other layers, similar formulation can be followed.

III. SIMULATION AND EXPERIMENTAL RESULTS

As mentioned earlier, to demonstrate the efficacy of the technique small cross-sectioned cylinders (in cross-section representing a point target) are used in this investigation. For obtaining simulation results, CST Microwave Studio® was used to generate wideband received signal data, for 101 frequency points in the X-band frequency range of 8.2-12.4 GHz. The number of observation angles used was 120 (one sample point for every 3 degrees), satisfying (34). The radii of the scanned first layer "aperture", the outer surface (second layer) and the inner surface (the third layer) of the circular dielectric object (see Fig. 1b) were 180 mm, 115 mm and 85 mm, respectively. The polarization direction used in this simulation and the experiment both were vertical polarization. The background medium (first layer) was assumed to be free-space. For this three-layer C-SAR imaging structure, the following relative dielectric constants ε_r, of 1, 2 and 4-j0.01 were taken for each layer, respectively. As shown in Figs. 2a-b, two small metallic cylinders each with a radius of 2 mm and length of 20 mm were considered as targets to be detected with this method. This cylindrical target geometry was used can be seen as a small target (smaller than a quarter wavelength) along the circular cross-section. For Fig. 2a, the positions of these two targets were at a radius of r = 6.5 cm with relative angular separation of 135 degrees (both targets are located in the inner layer). For Fig. 2b, the positions of these two targets were at a radius of r = 6.5 cm (located in the inner layer) and 10 cm (located in the outer layer), respectively, with relative angular separation of 135 degrees.

Figs. 2c-d corresponding to Figs. 2a-b respectively show the imaging results using the method proposed in this paper which considers multi-layer model. Figs. 2e-f show the imaging results of the method which uses free-space to approximate/replace the imaging domain background and does not consider the multi-layer model. Figs. 2g-h show the imaging results for when using average permittivity of all layers to approximate/replace the imaging domain background and does not consider the multi-layer model. Therefore, the results in Figs. 2e-h do not consider transmission and refraction model discussed in Section II-A, and the electromagnetic wave velocity, which is related to the permittivity of the assumed/replaced imaging domain background, is different.

However, the results in Figs. 2c-h are based on the same time-reversal SAR algorithm and only the model parameters (assumed/replaced imaging background) are changed yielding different results. It is clear that the results, using the outlined formulation, show properly-focused images of each object. On the other hand, the methods based on approximations of free-space or average background medium produce inferior images. These images are cluttered, unfocused, and with improper target locations, in particular for the point targets located in the inner layer. Considering the 3-dB width of the target image as resolution, the targets in the innermost layer of Fig. 2c have a resolution of ~12 mm along the radial direction and ~4 mm in the perpendicular direction. The target in the second layer (Fig. 2d) has a resolution of ~22 mm along the radial direction and ~4 mm perpendicular direction.

As mentioned earlier, unlike the Green's function approach (i.e., [28]) the utility of this approach is not limited to symmetrical layered cylindrical cases and can be applied to asymmetrical cases as well. To illustrate the efficacy of the approach for this purpose two asymmetrical layered cylindrical cases were considered, as show in Figs. 3a-b. The relative dielectric constant for each layer is 1, 2.2 and 2.6-j0.3, respectively. The radii of the scanned first layer "aperture", the outer surface (second layer) and the inner surface (the third layer) of the circular dielectric object (see Fig. 1b) were 180 mm, 115 mm and 85 mm, respectively. However, the inner cylinder was offset from the center (to the left) by 15 mm (Fig. 3a) and 10 mm (Fig. 3b), respectively. The same two targets were considered for these cases as well. The positions of these two targets were at a radius of $r = 6.5$ cm with relative angular separation of 90 degrees (both targets are located in the inner layer). As in the previous case (i.e., symmetrical cylinders), Figs. 3c-d show the imaging results of the inner layer using the multi-layer time reversal method proposed in this paper which considers the offset between the center positions of the inner layer and scanned aperture. For comparison, Figs. 3e-f show the imaging results of the inner layer using the multi-layer time reversal method proposed in this paper which does not consider this offset. Figs. 3g-h show the imaging results of the inner layer for when using average permittivity of all layers to approximate the imaging domain background and does not consider the multi-layer model. It is clear that the results, using the formulation outlined here, show properly-focused images of each object. On the other hand, and as in the previous case, the methods based on approximations of average background medium produce inferior images. However, we can determine the 3-dB width of the target image (i.e., images slice at the location of the targets), in the azimuthal and radial directions, and use these values to compare the results of Figs. 3c-f, as listed in Table I. The results reveal a clear advantage of the time-reversal approach when the offset of the center positions of the inner layer and scanned aperture is considered compared to the other two approaches.

In Fig. 3, there is a ring at the boundary but it does not appear in Fig. 2. This is thought to be due to subtracting the average reflection data from the measurements which removes all reflections of the boundaries that are constant due to symmetry.

For Fig. 3 there is no symmetry and thus the reflections are not constant and are not completely removed in this process. The multiple reflections between the boundaries that are not modeled in this technique, are also constant in the symmetric case and not constant in the asymmetric case, contributing to this effect.

The experimental setup to verify the results of this formulation is shown in Fig. 4. In this figure, a high-density polyethylene (HDPE) pipe was filled with dry and fine sand (less than ~1 mm in diameter). This sand could be seen as a homogeneous material, compared to the operating wavelength (~18.6 mm at 10 GHz in sand). The experiment was conducted at room temperature. Similar to the simulations above, two metallic screws with a diameter of 5 mm and length of 60 mm are placed inside the sand at different heights, representing two targets. During the actual measurements, this HDPE pipe was completely filled with sand covering (visually hiding) both screws. The pipe was then placed on a turntable and an open-ended rectangular waveguide, at X-band (8.2-12.4 GHz) was used to transmit the incident signal and also receive the reflected signal. An HP8510C Vector network analyzer (VNA) was used to generate incident and measure the received signals. The measurement parameters setup such as the frequency band, frequency sampling number and the angular sampling points were chosen to coincide those used in the simulation. The radius of the scanned aperture was 250 mm. In this experiment, the HDPE pipe was also scanned along the z-direction resulting in a cylindrical SAR image of the pipe. Twenty-one measurement points were samples along the z-axis with a spacing of $\Delta z = 5$ mm resulting in a total of 21x120 samples. The HDPE pipe had a thickness of 20 mm, with an inner radius of 73 mm. The HDPE was assumed lossless with a relative permittivity of $\varepsilon_r = 2.2$ [25]. The complex dielectric constant of sand was measured at X-band to have in average value (over the band) of $\varepsilon_r = 2.6 - j$0.3 [33]. Fig. 5a shows the 3D perspective view of the volume within the pipe (i.e., inner layer) of the two targets, indicating their relative positions and geometry (the scan in the height direction did not completely cover the lower target, as shown). Figs. 5b-c show cross-section image slices at the location of each target. These images clearly show the presence and correct locations of the two targets, as expected.

In order to corroborate the experimental results shown in Fig. 5, a new simulation was performed using the same parameters (radii and permittivities of each layer). To save calculation time, the two metallic cylindrical targets were placed at the same height. The positions of these two targets were at a radius of $r = 5.3$ cm (i.e., both targets are located in the inner layer) with a relative angular separation of 135 degrees. Fig. 6 shows the results of this simulation which closely matches the results shown in Figs. 5b-c.
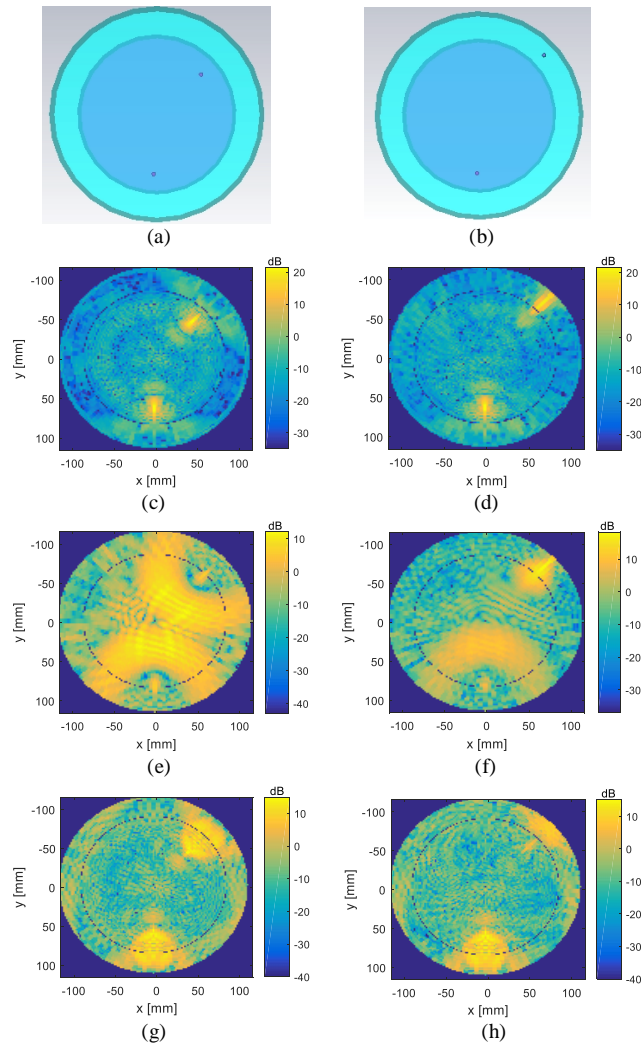
Fig. 2 CST simulation models and reconstructed images based on numerically simulated data for three-layer circular SAR: (a) CST simulation model of two point targets both located in the inner layer, (b) CST simulation model of two point targets located in inner layer and outer layer, (c) imaging result of (a) using the method proposed in this paper which considers multi-layer model, (d) imaging result of (b) using the method proposed in this paper which considers multi-layer model, (e) imaging result of (a) using the imaging method based on free-space background approximation, (f) imaging result of (b) using the imaging method based on free-space background approximation, (g) imaging result of (a) using the imaging method based on average-permittivity background approximation, and (h) imaging result of (b) using the imaging method based on average-permittivity background approximation.
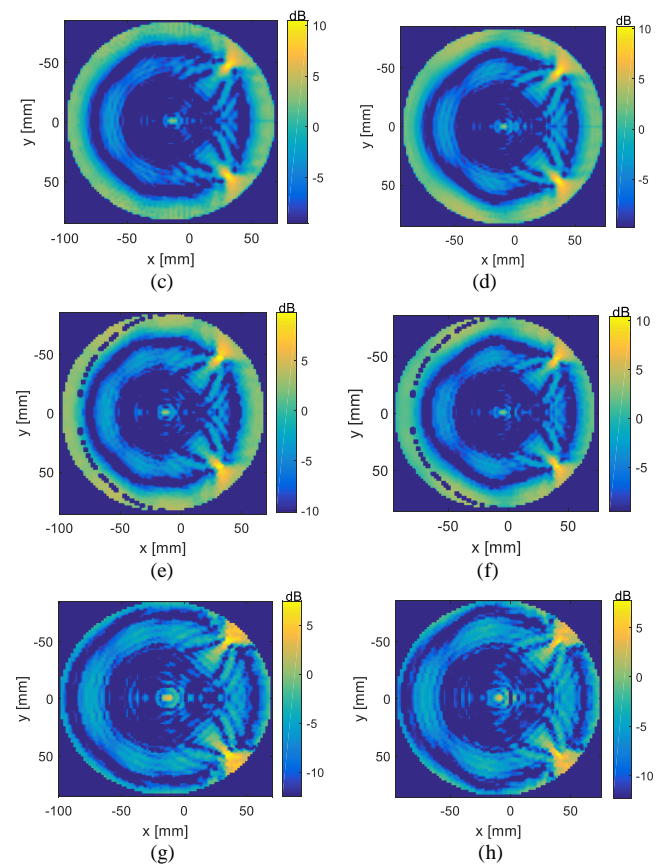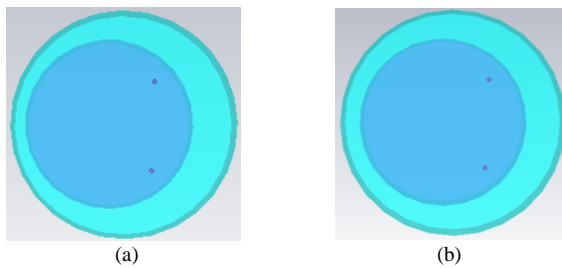

Fig. 3 CST simulation model and reconstructed images based on numerically simulated data when the center position of inner layer has an offset with that of the scanned aperture: (a) CST simulation model when this offset is 15 mm, and (b) when the offset is 10 mm. Multi-layered time reversal circular SAR imaging results when the offset is considered: (c) for 15 mm, and (d) for 10 mm. Multi-layered time reversal circular SAR imaging result when the offset is not considered: (e) for 15 mm, and (f) for 10 mm. The imaging results based on average-permittivity background approximation: (g) for 15 mm, and h) for 10 mm.

Table I. Azimuthal and radial widths calculated from results shown in Fig. 3c-f.

	Perpendicular 3-dB width (mm)	Radial 3-dB width (mm)
Fig.3 (c)	6	9
Fig.3 (d)	6	9
Fig.3 (e)	10	14
Fig.3 (f)	6	12
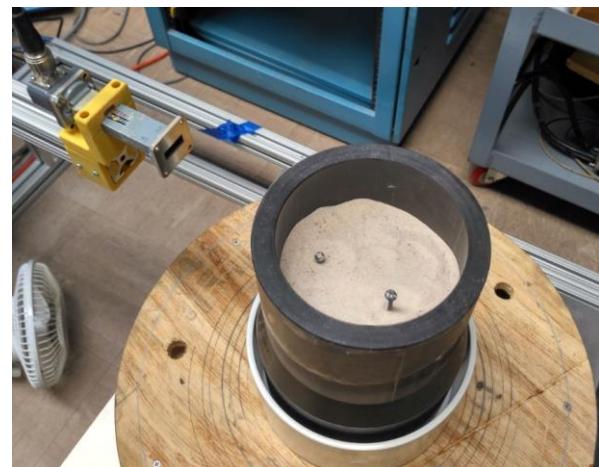
Fig. 4. HDPE pipe with two screws before being completely filled by sand.

the ability to correctly detect, locate and image these small embedded targets. This technique can address a number of practical imaging issues in nondestructive evaluation realm, and can also be applied to an arbitrary measurement domain and an arbitrary shape object.
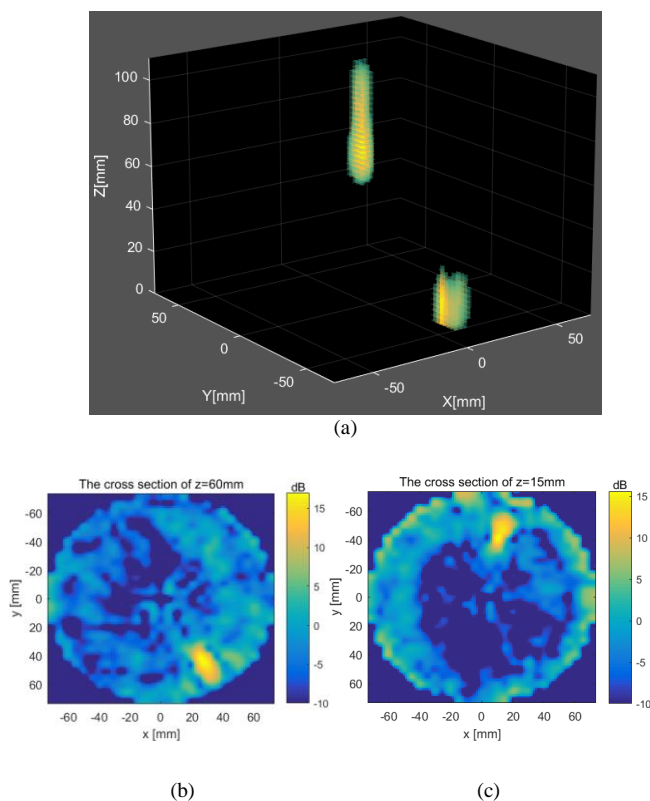

(a)

(b)   (c)

Fig. 5. 3D cylinder SAR image of two targets inside an HDPE pipe full of sand (the inner layer): (a) perspective view, (b) cross-section slice image of $z = 60$ mm and (c) cross-section slice image of $z = 15$ mm.
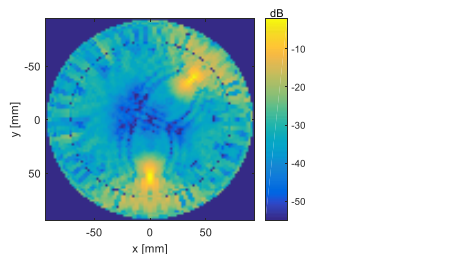

Fig. 6. Reconstructed image based on CST (numerically) simulated data for a three-layer circular SAR using the same parameters setup (radii and permittivities of each layer) used in the real experiment (in Fig. 5).

IV.   CONCLUSION

An imaging approach, for multi-layered circular and cylinder structures, based on electromagnetic time reversal SAR approach, has been outlined in this paper. In this approach, different transmission paths in different layers and the refraction at the boundaries between different layers are considered. This allows for generating images in which an object is properly located with a focused image. This approach readily addresses imaging needs for asymmetrical cylindrical objects as well. Numerical electromagnetic simulations (using CST Microwave Studio®) were used to check the efficacy of the technique for symmetrical and asymmetrical layered circular cylindrical structure. Subsequently, actual experiment was conducted at X-band (8.2-12.4 GHz) to produce images of embedded small targets for a layered cylindrical case involving an HDPE pipe filled with sand. These results also demonstrated

REFERENCES

[1] D. M. Sheen, D. L. McMakin, and T. E. Hall, "Three-dimensional millimeter-wave imaging for concealed weapon detection," *IEEE Trans. Microw. Theory Techn.*, vol. 49, no. 9, pp. 1581-1592, Sep. 2001.

[2] J. M. Lopez-Sanchez and J. Fortuny-Guasch, "3-D radar imaging using range migration techniques", *IEEE Trans. Antennas Propag.*, vol. 48, no. 5, pp. 728–737, May 2000.

[3] S. S. Ahmed, et al, "Advanced microwave imaging." *IEEE microwave magazine*, vol. 13, no. 6, pp. 26-43, Sep. –Oct. 2012.

[4] M. Fallahpour, et al, "Piecewise and Wiener filter-based SAR techniques for monostatic microwave imaging of layered structures," *IEEE Trans. Antennas Propag.*, vol. 62, no. 1, pp. 282-294, Jan. 2014.

[5] M.T. Ghasr, J.T. Case, and R. Zoughi, "Novel Reflectometer for Millimeter Wave 3D Holographic Imaging," *IEEE Trans. on Instrum. and Meas.*, vol. 63. No. 5, pp. 1328-1336, May 2014.

[6] O. Frey, and E. Meier, "3-D time-domain SAR imaging of a forest using airborne multibaseline data at L-and P-bands," *IEEE Trans. on Geosci. Remote Sens.,* vol. 49, no. 10, pp. 3660-3664, Oct. 2011.

[7] M. Soumekh, "Reconnaissance with slant plane circular SAR imaging," *IEEE Trans. Image Process.,* vol. 5, no. 8, pp. 1252-1265, Aug. 1996.

[8] K. E. Dungan, and L. C. Potter, "3-D imaging of vehicles using wide aperture radar," *IEEE Trans. Aerosp. Electron. Syst.,* vol. 47, no. 1, pp. 187-200, Jan. 2011.

[9] Z. Zhang, H. Lei, and Z. Lv, "Vehicle Layover Removal in Circular SAR Images via ROSL," *IEEE Geosci. Remote Sens. Lett.,* vol. 12, no. 12, pp. 2413-2417, Dec. 2015.

[10] M. L. Bryant, L. L. Gostin, and M. Soumekh, "3-D E-CSAR imaging of a T-72 tank and synthesis of its SAR reconstructions," *IEEE Trans. Aerosp. Electron. Syst.*, vol. 39, no. 1, pp. 211-227, Jan. 2003.

[11] O. Ponce, et al, "Fully polarimetric high-resolution 3-D imaging with circular SAR at L-band," *IEEE Trans. on Geosci. Remote Sens.*, vol. 52, no. 6, pp. 3074-3090, Jun. 2014.

[12] G. Jia, et al, "Fourier-based 2-D imaging algorithm for circular synthetic aperture radar: Analysis and application," *IEEE J. Sel. Topics Appl. Earth Observ.*, vol. 9, no. 1, pp. 475-489, Oct. 2016.

[13] Olivadese, Domenico, et al, "Near field 3D circular SAR imaging," *synthetic aperture radar (APSAR), Proceedings of the 3rd International Asia-Pacific Conference on. IEEE*, 2011.

[14] D. E. Lawrence, and K. Sarabandi, "Acoustic and electromagnetic wave interaction: Analytical formulation for acousto-electromagnetic scattering behavior of a dielectric cylinder," *IEEE Trans. Antennas Propag.*, vol. 49, no. 10, pp. 1382-1392, Oct. 2001.

[15] Buerkle, and K. Sarabandi, "Non-destructive evaluation of elastic targets using acousto-electromagnetic wave interaction and time reversal focusing," *IEEE Trans. Antennas Propag.,* vol. 57, no. 11, pp. 3628-3637, Nov. 2009.

[16] S. M. Moghadasi, and M. Dehmollaian. "Buried-object time-reversal imaging using UWB near-ground scattered fields," *IEEE Trans. on Geosci. Remote Sens.*, vol. 52, no. 11, pp. 7317-7326, Nov. 2014.

[17] M. Abduljabbar, et al. "Continuous wavelet transform-based frequency dispersion compensation method for electromagnetic

time-reversal imaging," *IEEE Trans. Antennas Propag.*, vol. 65, no. 3, pp. 1321-1329, Mar. 2017.

[18] C. Odedo, et al, "Time Reversal Technique Based on Spatiotemporal Windows for Through the Wall Imaging," *IEEE Trans. Antennas Propag.,* vol. 65, no. 6, pp. 3065-3072, Jun. 2017.

[19] M. Fink, "Time reversal of ultrasonic fields. I. Basic principles," *IEEE Trans. Ultrason., Ferroelectr., Freq. Control,* vol. 39, no. 5 pp. 555-566, Sep. 1992.

[20] J. B. Harley, and J. M. F. Moura, "Broadband localization in a dispersive medium through sparse wavenumber analysis," *Proceedings of Acoustics, Speech and Signal Processing (ICASSP), IEEE International Conference on*, 2013.

[21] D. L. McMakin, et al, "Dual-surface dielectric depth detector for holographic millimeter-wave security scanners," *R. Appleby and DA Wikner, Eds* 7309.1 (2009): 73090G.

[22] D. L. McMakin, T. E. Hall, and D. M. Sheen, "Holographic radar imaging privacy techniques utilizing dual-frequency implementation," *Proc. of SPIE,* Vol. 6943, 2008.

[23] O. Ponce, et al, "First airborne demonstration of holographic SAR tomography with fully polarimetric multicircular acquisitions at L-band," *IEEE Trans. on Geosci. Remote Sens.*, vol. 54, no. 10, pp. 6170-6196, Oct. 2016.

[24] M.T. Ghasr, M.J. Horst, M. Lechuga, R. Rapoza, C. Renoud and R. Zoughi, "Accurate One-Sided Microwave Thickness Evaluation of Lined-Fiberglass Composites," *IEEE Trans. on Instrum. and Meas.*, vol. 64, no. 10, pp. 2802-2812, October 2015.

[25] B. Riddle, J. Baker-Jarvis, and J. Krupka, "Complex permittivity measurements of common plastics over variable temperatures," *IEEE Trans. Microw. Theory Tech.*, vol. 51, no. 3, pp. 727–733, Mar. 2003.

[26] M. Fallahpour, and R. Zoughi, "Fast 3-D qualitative method for through-wall imaging and structural health monitoring," *IEEE Geosci. Remote Sens. Lett.*, vol. 12, no. 12, pp. 2463-2467, Dec. 2015.

[27] H. Jung, and K. Kim, "Autofocusing Technique Based on Generalized Multilayer Stolt Migration," *IEEE Trans. on Geosci. Remote Sens.,* Nov. 2017.

[28] Laviada, J., B. Wu, M.T. Ghasr, and Reza Zoughi, "Nondestructive Evaluation of Microwave-Penetrable Pipes by Synthetic Aperture Imaging Enhanced by Full-Wave Field Propagation Model", *IEEE Trans. on Instrum. and Meas.*, vol. 68, no. 4, pp. 1112-1119, Apr. 2019.

[29] T. Mobashsher, A. Mahmoud, and A. M. Abbosh, "Portable wideband microwave imaging system for intracranial hemorrhage detection using improved back-projection algorithm with model of effective head permittivity," *Scientific reports,* vol. 6, 2016.

[30] Y. Wang, et al, "Synthetic bandwidth radar for ultra-wideband microwave imaging systems," *IEEE Trans. Antennas Propag.*, vol. 62, no. 2, pp. 698-705, Feb. 2014.

[31] C. A. Balanis, *"Advanced engineering electromagnetics,"* John Wiley & Sons, 1999.

[32] M. Soumekh, "Synthetic aperture radar signal processing," *New York: Wiley*, 1999.

[33] Bois, K., A. Benally and R. Zoughi, "An Exact MultiMode Solution for the Reflection Properties of an Open-Ended Rectangular Waveguide Radiating into a Dielectric Half-Space: Forward and Inverse Problems," *IEEE Trans. on Instrum. and Meas.*, vol. 48, no. 6, pp. 1131-1140, December 1999.